Polysialosides outperform sulfated analogs for the inhibition of SARS-CoV-2

Vinod Khatri,[1,2] Nico Boback,[1,4] Hassan Abdelwahab,[6] Daniela Niemeyer,[5] Tahlia M. Palmer,[4] Anil Kumar Sahoo,[6*] Yannic Kerkhoff,[7,8] Kai Ludwig,[7] Dilara Balci,[1] Jakob Trimpert,[9] Rainer Haag,[1] Tatyana L. Povolotsky,[10] Roland R. Netz,[6] Christian Drosten,[5] Daniel C. Lauster,[4*] Sumati Bhatia[3*]

[1]*Institute for Chemistry and Biochemistry, Freie Universität Berlin, Takustr. 3, Berlin 14195 Germany*

[2]*Department of Chemistry, TDL Govt. College for Women Murthal, Sonipat-131027, Haryana, India*

[3]*Faculty of Science and Engineering, Department of Chemistry, Swansea University, Singleton Campus, Swansea SA28PP, United Kingdom*

[4]*Institute of Pharmacy, Biopharmaceuticals, Freie Universität Berlin, Kelchstr. 31, 12169 Berlin*

[5]*Institute of Virology, Campus Charité Mitte, Charité - Universitätsmedizin Berlin, German Center for Infection Research, associated partner Charité, Berlin, Germany*

[6]*Department of Physics, Freie Universität Berlin, Arnimallee 14, 14195 Berlin, Germany*

[7] *Forschungszentrum für Elektronenmikroskopie, Core-Facility BioSupraMol, Institute of Chemistry and Biochemistry, Freie Universität Berlin, Fabeckstraße 36a, 14195 Berlin, Germany*

[8] *Zuse-Institut Berlin (ZIB), Takustraße 7, 14195 Berlin, Germany*

[9] *Department of Pathobiology and Diagnostic Medicine, Kansas State University, 1800 Denison Avenue, Manhattan, KS, 66506, USA*

[10]*SupraFAB, Institute for Chemistry and Biochemistry, Freie Universität Berlin, Altensteinstr. 23a, 14195 Berlin, Germany*

*Corresponding authors:

Sumati Bhatia, Email: sumati.bhatia@swansea.ac.uk

Daniel Lauster, Email: daniel.lauster@fu-berlin.de

Anil Kumar Sahoo, Email: aksahoo@zedat.fu-berlin.de

Abstract

Both polysialosides and polysulfates are known to interact with the receptor binding domain (RBD) of the SARS-CoV-2 spike protein. However, a comprehensive site by site analysis of

their binding affinities and potential synergistic antiviral effects have not been performed. Here, we report on the synthesis of polysialosides with nanomolar binding affinities to spike proteins of SARS-CoV-2 in solution using microscale thermophoresis (MST). The dendritic polyglycerol based polysialosides $dPG_{500}(SA)_{0.55}$ and $dPG_{500}(SA)_{0.25}$, with a dissociation constant K_d of 4.78 nM and 10.85 nM, respectively, bind ~500 times stronger than the high density polysulfated analog $dPG_{500}(OSO_3Na)_{0.55}$, to intact SARS-CoV-2 virus particles or isolated spike protein. In fact, the presence of sulfate groups in a heteromultivalent compound $dPG_{500}(SA)_{0.20}(OSO_3Na)_{0.20}$ weakens the binding to spike proteins. A polycarboxylated analog does not bind to SARS-CoV-2, ruling out that the interaction of polysialoside is simply driven by electrostatic interactions. Furthermore, we found potent nanomolar binding of $dPG_{500}(SA)_{0.55}$ to SARS-CoV-2 variant B.1.617 (Delta) and B.1.1.529 (Omicron) RBD. Using explicit-solvent all-atom molecular dynamics (MD) simulations and docking studies, we obtain atomistic details on the interaction of different functional groups with the SARS-CoV-2 RBD and their binding affinities. Our data support the conclusion that sialosides interact stronger with RBD than sulfates. Notably, our most affine binder $dPG_{500}(SA)_{0.55}$ inhibits SARS-CoV-2 (WT, D614G) replication up to 98.6% at low nanomolar concentrations.

Introduction

The coronavirus disease COVID-19, caused by the severe acute respiratory syndrome coronavirus 2 (SARS-CoV-2), which was first reported in Wuhan (China) in 2019, led to an acute global pandemic, with more than 776 million confirmed cases and over 7.0 million deaths (as of September 2024).[1] Since the rise of SARS-CoV-2 there has been a great interest in understanding SARS-CoV-2 virus attachment and entry into host cells. SARS-CoV-2 is roughly globular with a diameter in the range of 80-120 nm, resulting in a surface area of 20-45 μm^2.[2] The viral membrane contains viral spike (S)-glycoproteins, which are homotrimers consisting of S1 and S2 subunits. The S1 subunit of the (S)-protein carries the receptor binding domains (RBD) that binds to the human angiotensin converting enzyme 2 (hACE2) on the surface of hosts cells, which mediates viral uptake.[3]

Many viruses exploit sialylated or sulfated glycans on cell membranes as a primary attachment factor before binding to specific membrane-protein receptors needed for cell entry. During evolution of SARS-CoV-2 especially the role of polysulfates, such as glycosaminoglycans (GAG) became more important for viral attachment. This can be observed by an increased abundance of cationic amino acids on the RBD.[4, 5] The RBD has a binding site for heparan sulfate lateral to the ACE2 binding site.[6] Blocking of one or the other site of RBD with decoy structures has been demonstrated to be effective for virus inhibition.[6][8] Interestingly,

besides the relevance of sulfates, sialylated glycans were found to act as co-receptors for the virus attachment. Saso and coworkers reported on the reduction of infection by SARS-CoV-2 after enzymatic removal of cell surface sialic acids or using lipidated 2,6-sialyllactose linked to polyglutamic acid as a competitor for SARS-CoV-2 attachment to the host cell.[9] Further, Nguyen et al. screened defined glycan libraries for binding with SARS-CoV-2 RBD and spike proteins using a catch and release ESI-MS technique. They observed micromolar affinities of SARS-CoV-2 RBD interacting with sialylated glycolipids, thereby facilitating viral entry.[10] Baker and coworkers even achieved apparent K_d values of 1 nM using surface plasmon resonance studies when highly sialylated glyconanoparticles were titrated against SARS-CoV-2.[11] Another group around Petitjean observed a significant decrease in the infection of A549 cells by SARS-CoV-2 pseudoviruses at 10 µM using porphyrin-based 9-*O*-acetyl sialoside oligomers.[12]

These observations on the interaction of SARS-CoV-2 RBD with sialosides and sulfates inspired us to explore different variants of polysialosides, polysulfates or hybrid materials displaying both functional entities. Using such defined nanostructures would not only have implications on virus inhibition, but also on the virus binding capability and preference towards sialosides or sulfates. As the receptor binding site for a sialoside has not been identified yet, one could identify from binding studies whether the binding sites overlap or are spatially separated. Thus, both functional groups could compete with each other or act synergistically.

Therefore, the study in hand investigates their role in SARS-CoV-2 binding using dendritic polyglycerol (dPG) as carrier systems with similar sizes, geometry, and varying ligand densities (high and low). Also, both sialic acid and sulfate covalently linked to the same polymer has been explored. These polymer nanoparticles were then analyzed biophysically by means of MST with regard to their binding affinities towards different domains, namely the RBD or S1 subunit of SARS-CoV-2 S-protein. For this purpose, multivalent sulfated and sialylated dendritic polyglycerols [dPG(OSO_3Na) and dPGSA], as well as heteromultivalent dPGs presenting both sialosides and sulfates [dPGSA(OSO_3Na)] were tested to bind to SARS-CoV-2 (WT, D614G). To investigate whether the aromatic group at the anomeric position of sialic acid contributes to its interaction with RBD, a polyglycerol-based multivalent nanoparticle bearing aromatically modified sialosides [dPG(SA_{aryl})] was synthesized. Because each sialoside has one carboxylic acid group, a carboxylated PG analog [dPG(COOH)] was also explored to examine the role of isolated carboxylic acid groups for the SA-RBD interactions and to identify the importance of the electrostatic interaction. This was followed by MD simulations and docking studies to not only rationalize these binding behaviors but also to understand competition mechanisms of carboxylates, sulfates, and sialosides for their binding to RBD. We then conducted affinity measurements using MST of polymer

nanoparticles against wild-type SARS-CoV-2. Those nanoparticles with a detectable dissociation constant (K_d) were further studied for their antiviral efficacy using entry inhibition assays on Calu-3 cells. Virus titers were assessed 24 and 48 h post infection (hpi) using qPCR. In the presence of the highly sialylated polyglycerol $dPG_{500}SA_{0.55}$, SARS-CoV-2 infection was inhibited up to 98.6%. The interaction of polyglycerol sialosides with SARS-CoV-2 particles was further investigated and visualized by cryo-electron tomography (cryo-ET). Overall, our study identified highly sialylated polyglycerols as potential antivirals for inhibition of infection at early as well as later stages of SARS-CoV-2 infection. Additionally, our nanoparticles also provide evidence for the competition among sulfate and sialoside when they are presented together on dendritic polyglycerol for their binding with SARS-CoV-2 spike proteins.

Results and Discussions

Design, synthesis and characterization of polyglycerol-based nanoparticles

The SARS-CoV-2 spike (S)-protein is a homotrimeric membrane protein with a globular head domain, being S1, and the stem region S2, which is required for fusion with the host cell membrane. The head domain S1 can be further divided into the N-terminal domain (NTD) and the RBD, which interacts with ACE2 and attachment factors such as sulfates or sialosides. The RBD interacts with ACE2 via the receptor binding motif (RBM, see also Figure 1). From the crystal structure of complete S-proteins an intra-trimeric distance between the center of RBDs of 4 and 8.9 nm could be determined when the RBD on the trimer is in down (PDB 7DF3) or up-right (PDB 7CAK) conformation, respectively (Figure 1). In order to increase the functional valency, i.e. the successful bridging of more than one RBD- whether in upright or down conformation, we selected a 500 kDa dendritic polyglycerol (dPG_{500}) with a hydrodynamic diameter (D_h) of 13.21 nm. The high density of surface hydroxy groups, ~21 -OH groups per nm^2, allows further functionalization. The dPG_{500} was sialylated in three steps, according to a previously reported procedure, using a copper-catalyzed Sharpless-Huisgen click reaction [12] to yield $dPG_{500}SA_{0.25}$ and $dPG_{500}SA_{0.55}$. For comparison, polysulfated analogs $dPG_{500}(OSO_3Na)_{0.25}$ and $dPG_{500}(OSO_3Na)_{0.55}$ were obtained with similar densities of functionalities according to a known sulfation protocol (see Supporting Information). Polysulfates were reported to bind with the lateral cationic patch on the RBD of SARS-CoV-2 spike proteins [8]. Also, a recent study showed that self-assembled polycarboxylated double layered sheets (up to >400 nm) could interact with S-proteins via electrostatics [14]. Therefore, to investigate the role of carboxylic acid groups of sialic acids in dPGSAs for SARS-CoV-2 binding, a polycarboxylated analog $dPG_{500}COOH_{0.20}$ with similar size and ζ-potential as $dPG_{500}SA_{0.25}$ was synthesized, serving as control. We found previously that heteromultivalent

polyglycoside systems that target both hemagglutinin (HA) and neuraminidase (NA) of influenza A virus (IAV) are superior to homomultivalent compounds that target only HA or NA,[15] we wanted to transfer the concept of heteromultivalency on SARS-CoV-2. However, in this case we want to target only one viral protein, but with different ligands, and synthesized the nanosystem $dPG_{500}SA_{0.20}(OSO_3Na)_{0.20}$ having both sialoside and sulfate groups on one dPG scaffold.

All polymer conjugates based on dPG_{100} or dPG_{500} showed hydrodynamic diameters between 10 - 14 nm. Important to note is that the polysulfated and polysialylated analogs were similar in size, ligand density, and ζ-potentials. For $dPG_{500}(OSO_3Na)_{0.25}$ and $dPG_{500}SA_{0.25}$ hydrodynamic diameters of D_h 13.3 and 14.6 nm, and ζ-potentials of -26.2 and -28.2 mV respectively, were determined. For $dPG_{500}(OSO_3Na)_{0.55}$ and $dPG_{500}SA_{0.55}$ diameters of D_h 11.8 and 13.9 nm, and ζ-potentials -36.3 and -45.9 mV respectively, were assessed.

In another aspect, sialic acids bearing aromatic groups at C-2 position were found to be 8 - 64 times stronger inhibitors of influenza virus induced hemagglutination than α-methylsialoside.[16] To test whether an aromatic group at C-2 position of the sialoside could further enhance virus binding to SARS-CoV-2, a polysialoside with an aromatic modification at the C-2 position of sialic acid named $dPG_{100}(SA_{aryl})_{0.20}$, similar to the compound $dPG_{100}(SA)_{0.20}$, was synthesized (Scheme 1). All compounds were thoroughly characterized by spectroscopic techniques. Successful conjugation of sialosides or sulfates were determined by ^{1}HNMR and elemental analysis. The ζ-potentials and hydrodynamic diameters (D_h) of the polymers were determined in phosphate buffer (10 mM, pH 7.4) (Table 1, Figure S15 und S16, see Supporting Information for synthesis and characterization). Further physicochemical properties of additional polymer systems are given in Table 1.

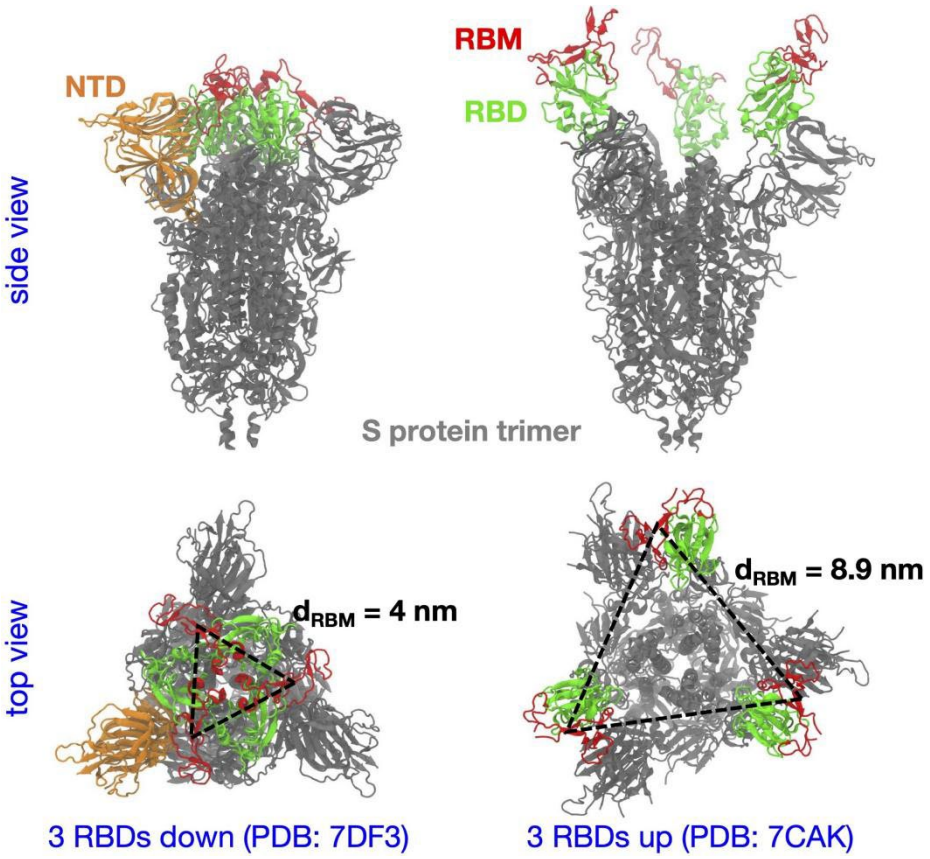

Figure 1: Deposited cryo-electron microscopy structures (see PDB entries) of the spike (S) protein trimer with all three RBDs in the down or up conformation shown in the left and right column, respectively. The S-protein is shown in grey, and the RBD in green except its receptor binding motif (RBM) that forms direct contacts with ACE2 is highlighted in red. The N-terminal domain (NTD) of one monomer of the S-protein is shown in orange only in the left column. The center-of-mass distance between two RBMs, d_{RBM}, is mentioned for each conformation.

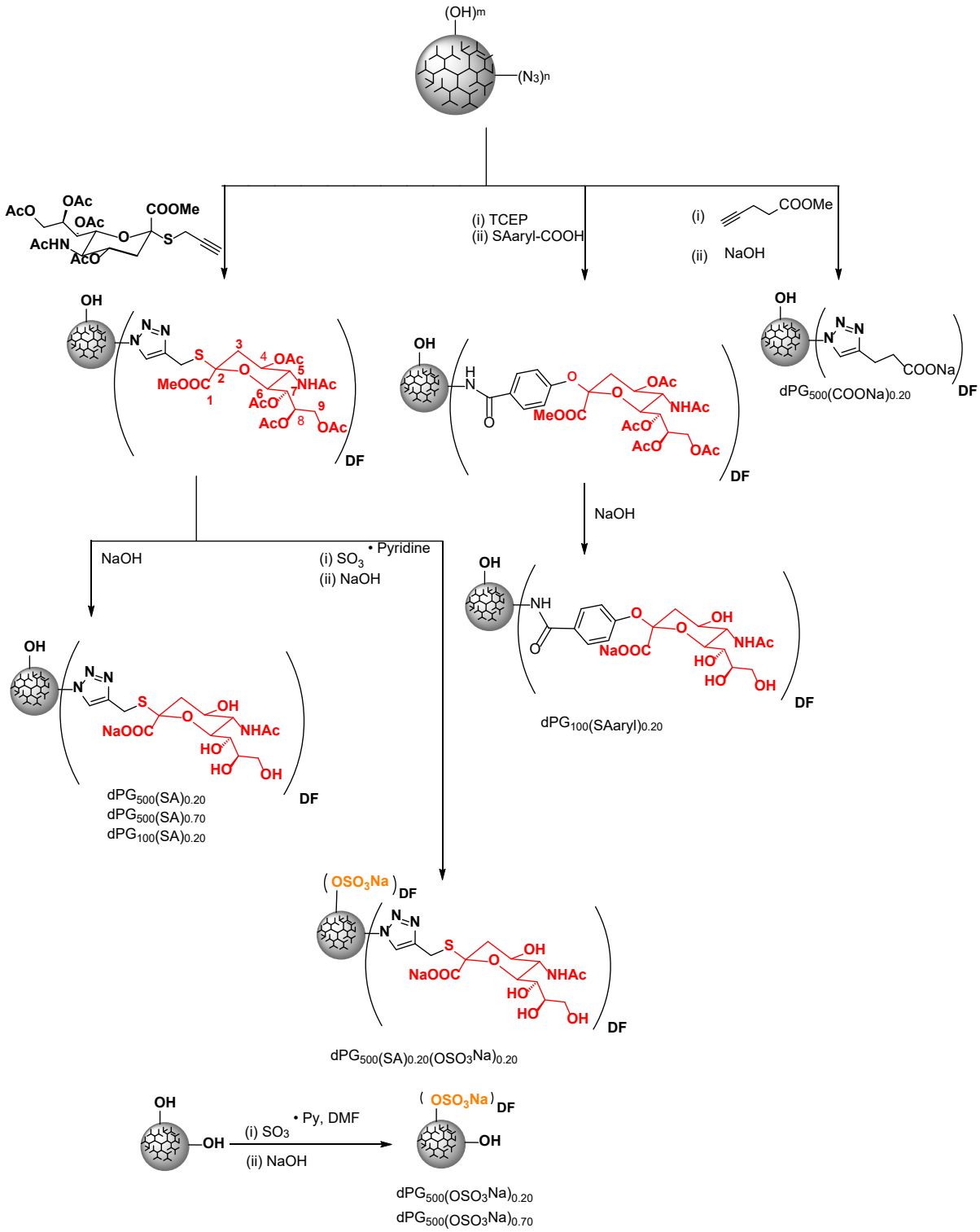

Scheme 1: Overview of synthesized multivalent nanoparticles carrying either sialosides, sulfates, carboxylates, or combinations thereof. (Synthesis details are provided in the Supporting Information)

Characterization

Table 1: Characterization of un-/functionalized dPG_{500} and dPG_{100}.

Compound[a] ($PG_{MW}SA_{DF}$)	SA or OSO_3Na/NP[b]	DF[c] (%)	D_h[d] (nm)	PDI[d]	SA or OSO_3Na /nm^2[e]	ζ-potential ± SD[f] [mV]
$dPG_{500}OH$	-	-	13.21 ± 0.41	0.35	-	-6.91 ± 1.67
$dPG_{500}SA_{0.25}$	1824	27	14.61 ± 0.18	0.17	2.72	-28.2 ± 1.44
$dPG_{500}SA_{0.55}$	3648	54	13.89 ± 0.21	0.43	6.10	-45.9 ± 2.76
$dPG_{500}COONa_{0.20}$	1300	20	14.02 ± 0.39	0.56	2.11	-22.1 ± 6.94
$dPG_{500}(OSO_3Na)_{0.25}$	1625	25	13.33 ± 0.25	0.39	2.88	-26.2 ± 6.47
$dPG_{500}(OSO_3Na)_{0.55}$	3575	55	11.40 ± 0.17	0.59	8.76	-36.3 ± 9.67
$dPG_{500}SA_{0.20}(OSO_3Na)_{0.20}$	2600	40	12.83 ± 0.17	0.53	2.52	-48.7 ± 7.64
$dPG_{100}OH$	-	-	10.18 ± 0.64	0.41	-	-6.68 ± 0.18
$dPG_{100}SA_{0.20}$	297	22	9.60 ± 1.12	0.59	1.02	-38.8 ± 0.95
$dPG_{100}(SAaryl)_{0.20}$	297	22	10.29 ± 0.62	0.57	1.02	-14.6 ± 2.78

[a]polymer structure is indicated by the molecular weight (MW) of the dendritic polyglycerol (dPG) backbone and the degree of functionalization (DF) of either sialic acid (SA), sulfate (OSO3Na) or carboxylic acid groups (COOH). [b]Number of SA units per polymer, calculated from DF as determined by ^{1}HNMR. DF is the percentage of total OH groups on dPG that were functionalized with the respective ligands. [c]Determined by ^{1}HNMR analysis. [d] Determined with DLS, measured in aqueous buffer solution (PB, pH 7.4), mean values of triplicates ± standard deviation of the volume distribution profile. [e]Average SA densities, on the surface of an assumed spherical dPG particle, calculated by the determined number of SA. [f] Determined surface potential by measuring triplicates of the zeta potential in aqueous buffer solution (PB, 10 mM, pH 7.4) together with standard deviation

Affinity characterization of polymer nanoparticles against SARS-CoV-2 spike proteins or whole virus particles

In order to determine the affinities of the synthesized nanoparticles, we conducted MST measurements. We demonstrated earlier that such binding measurements can also be performed with whole virus particles.[12] By this way, also multivalent binding events in equilibrium can be quantified by introducing an apparent dissociation constant ($K_{d,app}$). We first measured binding of the different polymers against whole SARS-CoV-2 B.1 (WT, D614G) particles. We found that polymers functionalized with SA i.e. $dPG_{500}SA_{0.25\ or\ 0.55}$, $dPG_{100}SA_{0.20}$ or its aromatic variant $dPG_{100}(SA\text{-}aryl)_{0.20}$ with nM K_d values had much stronger (~up to 1000 times) binding compared to the high-density sulfated versions $dPG_{500}(OSO_3Na)_{0.55}$ with K_d of 2.46 µM (Figure 2A, Table 1). The µM K_d values observed for polysulfates are in agreement with an earlier investigation reported by Nie *et al.*, in which high-density dendritic sulfated polyglycerol exhibited K_d of 144 µM against the RBD of wild-type SARS-CoV-2.[8] Interestingly, the heteromultivalent $dPG_{500}SA_{0.20}(OSO_3Na)_{0.20}$ showed with a K_d of 24.92 nM a similar binding affinity compared to the homomultivalent sialoside $dPG_{500}(SA)_{0.20}$ with only 2-fold lower K_d (10.85 nM) (Table 1). This indicates that statistically distributed sulfates in addition to sialosides on the dPG backbone did not strongly enhance binding to SARS-CoV-2 particles. Furthermore, the polycarboxylated analog $dPG_{500}COONa_{0.20}$ did not show binding with the SARS-CoV-2 B.1 (WT, D614G) indicating that sialic acid interactions with the SARS-CoV-2 are not merely electrostatic. Notably, introducing aromaticity on SA at the anomeric C2 position improved binding by a factor of about five, as demonstrated by $dPG_{100}(SA_{aryl})_{0.20}$

having a lower dissociation constant (K_d 14.22 nM) compared to $dPG_{100}SA_{0.20}$ (K_d 69.14 nM) (Figure 2C). All obtained values are listed in Table 2.

Based on these findings, we further probed the binding of the nanoparticles to defined domains of the S-protein of wild-type SARS-CoV-2. First, we characterized the recombinant RBD of the wild-type variant [SARS-CoV-2 (2019-nCoV)] which is known to interact with ACE2, heparan sulfate (HS) and a potential SA binding site. By testing polysialosides with significantly different SA densities, we found that $dPG_{500}SA_{0.55}$ enhanced the binding affinity to RBD [SARS-CoV-2 (2019-nCoV)] by approximately 11-fold more than scaffolds with lower SA density $dPG_{500}SA_{0.25}$ (K_d 7.15 nM and 80.11 nM), respectively. No significant binding was observed to the recombinant NTD protein of the wild-type variant SARS-CoV-2 (2019-nCoV) (Figure 2B, Table 2). This result indicates the absence of other binding sides for the sialosides outside of the RBD. Finally, multivalent $dPG_{500}SA_{0.55}$ bound equally effectively to the RBD protein of the Omicron variant (B.1.1.529) and had even an improved binding affinity to the full virus Delta variant (B.1.617) (Figure 2D-E, Table 2).

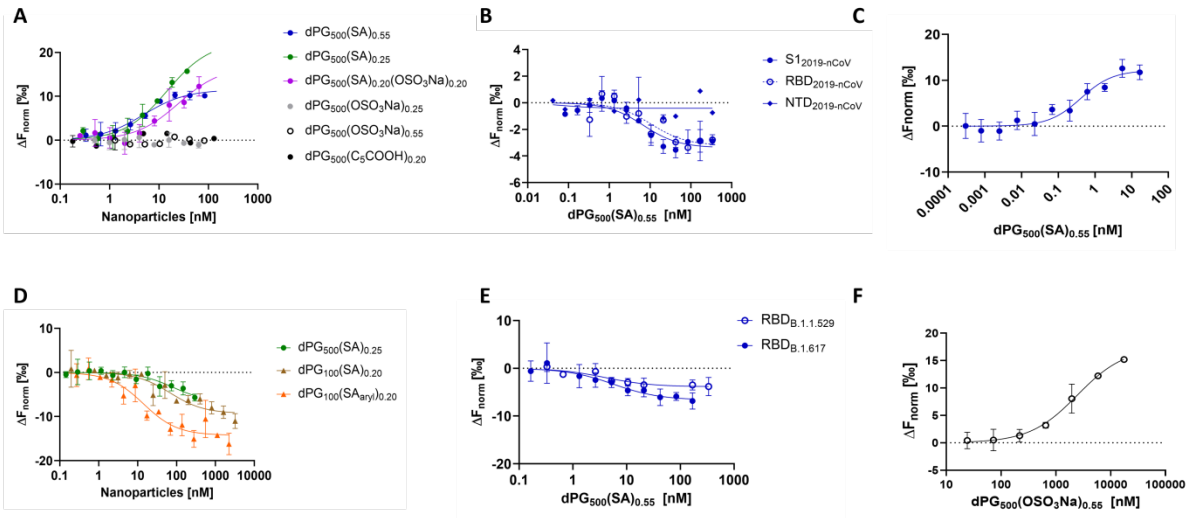

Figure 2: Affinity measurements using microscale thermophoresis with **A)** SARS-CoV-2 wild-type variant B.1 (WT, D614G) (full virus) against dPG-conjugates; **B)** Domains of the Spike protein from the wild-type variant against $dPG_{500}(SA)_{0.55}$; **C)** RBD protein from wild-type variant against $dPG_{500}(SA)_{0.25}$ with a 500 kDa backbone, $dPG_{100}(SA)_{0.25}$ with a 100 kDa backbone and $dPG_{100}(SAaryl)_{0.20}$; **D)** SARS-CoV-2 variant B.1.617 (Delta) (full virus) against $dPG_{500}(SA)_{0.55}$; **E)** $dPG_{500}(SA)_{0.55}$ against RBD proteins from B.1.617 (Delta) and B.1.1.529 (Omicron) variants; **F)** SARS-CoV-2 wild-type variant B.1 against $dPG_{500}(OSO_3Na)_{0.55}$ at higher nanoparticle concentrations. In A-F each data point represents biological repeats of N = 3. Data points were fitted with one sided fit assuming a 1:1 ligand to receptor ratio.

Table 2: Summary of dissociation constants ($K_{d,\ app,\ NP}$) using microscale thermophoresis (MST). The number of biological repeats for each binding interaction is N≥3. The error bar indicated the standard error. n.d. not detectable until 10 µM nanoparticles

Compound[a] ($PG_{MW}SA_{DF}$)	$K_{d,app}$ (nM)						
	Wild-type (full virus) B.1 (WT, D614G)	**S1 (WT)**	**RBD (WT)**	**NTD (WT)**	**Delta (full virus) B.1.617**	**RBD Delta B.1.617**	**RBD Omicron B.1.1.529**
$dPG_{500}(SA)_{0.55}$	4.78 ± 1.19	3.14 ± 2.89	7.15 ± 7.31	n.d.	0.42 ± 0.16	5.70 ± 1.82	3.98 ± 1.45
$dPG_{500}(SA)_{0.25}$	10.85 ± 2.65		80.11 ± 47.67			63.04 ± 51.2	
$dPG_{100}(SA)_{0.20}$	61.80 ± 26.64		69.14 ± 32.57				
$dPG_{100}(SAaryl)_{0.20}$	9.01 ± 13.97		14.22 ± 32.57				
$dPG_{500}(OSO_3Na)_{0.55}$	2466 ± 250.34*						
$dPG_{500}(SA)_{0.20}(OSO_3Na)_{0.20}$	24.92 ± 5.75						
$dPG_{500}(COOH)_{0.20}$	n.d.						
$dPG_{500}(OSO_3Na)_{0.25}$	n.d.						
6' - sialyllactose			n.d.				

*K_d values are given in terms of the nanoparticle (NP) concentration. WT is wild-type

Theoretical analysis: MD simulation and molecular docking

To understand the relevance of different functional groups of dPGs, we have performed explicit-solvent all-atom MD simulations of the SARS-CoV-2 spike protein RBD in solutions of different ligands. We have considered only the RBD in the simulations, as it is inferred from the MST measurements that sialylated dPGs predominantly interact with the RBD (Table 2). Though earlier experimental and simulation studies have suggested that SAs bind both to the NTD[16-19] and the RBD[20-22], SAs grafted to dPGs can form multivalent interaction with the RBD because of its larger solvent-accessible surface area, especially in the up-conformation. In addition, the NTD surface compared to the RBD, is highly shielded by glycans,[24] restricting its multivalent interaction with sialylated dPGs. For the functionalization with sulfate groups, our earlier studies have revealed that polysulfates interact mostly with the cationic patch on the RBD.[9, 24]

The simulation unit cell is shown in Figure 3A and details of the simulation method and data analysis are presented in the supporting information (SI). We observe that the monomer of sialic acid, i.e., N-acetylneuraminic acid (NANA), binds to the RBD via multiple binding modes, snapshots for the top five binding poses are shown in Figure 3D. The number of close contacts plot reveals that despite SA binding to different types of surface residues of RBD, it forms a greater number of contacts with cationic amino acids (Figure 3B). The number density plot,

however, shows that not only the anionic carboxylate group but also charge-neutral hydroxyl and carbonyl groups of SA have similar propensities towards the RBD (Figure 3C). Because of the additional interactions formed by SA, multivalent binding of polysialosides with one RBD can be formed. This could be rationalized based on the decrease in K_d values with increasing the degree of sialylation (see Table 2), which cannot be explained by a 1:1 SA:RBD ratio.

To understand whether the experimentally determined enhanced binding affinity of sialylated dPGs to the RBD, compared to sulfated ones, is due to only the carboxylate of SA or its additional functional groups as well, we check the competitive binding between carboxylate and sulfate groups by performing MD simulation of the RBD in a solution of BGLC (a derivative β-D-Glucose, taken from a Heparin monomer, with both carboxylate and sulfate groups) ligands. Number distributions of these two groups around RBD show a slightly greater number of carboxylates present near RBD, compared to sulfates (Figure 3E). Analysis of the residence time, i.e. the average duration for which a ligand stays within a close proximity to the RBD, for the carboxylate and sulfate group indicates a rather similar timescale for both functional groups: 12 ns for COO^- and 22 ns for SO_4^- (see Figure S21 and the discussion in the SI). Since the residence time is inversely proportional to the exponential of the binding free energy ΔG_b ($\Delta G_b \leq 0$), the above finding suggests that both functional groups bind to the RBD protein with approximately equal strength. Thus, other functional groups of SA apart from the carboxylate, as shown in Figure 3C, contributes significantly to strengthening the binding of SA to RBD. This finding further supports the hypothesis that the RBD contains binding sites for SA.

The MST measurements indicated that the linking groups at the anomeric position of SA (Scheme 1) influenced sialylated dPGs' dissociation constant, K_d, values and hence their binding free energy, ΔG_b, values since both are related as $\Delta G_b = RT\ln(K_d/c_0)$, where R is the ideal gas constant, T represents temperature, and the standard-state concentration $c_0 = 1$ mol/L. In particular, including an aryl group in the anomeric position of SA leads to a decrease in K_d and thus an increase in the binding affinity. To understand whether this arises from direct, favourable interactions of the aryl group with RBD or some other subtle effects, we have performed molecular docking studies (details provided in the SI) for SA, the -S-triazolyl and -O-aryl substituted SAs used in experiments. We found that the magnitude of the docking interaction energy of aryl substituted SA (Ar-SA) is higher than the thio-triazolyl functionalized SA (Thio-SA) for the top nine docking poses (Figure 3F). Compared to SA, both Ar-SA and Thio-SA interact more strongly with RBD because of their additional functional groups. Interestingly, all three variants of SA bind to the receptor binding motif (RBM), the part of RBD that forms direct contact with the ACE2 receptor protein on the host cell, as seen from

the best docking poses in Figure 3G. The SA binding sites obtained from the docking studies match with “top 4” and “top 5” binding poses of SA obtained from the MD simulation (Figure 3D). This signifies that the docking scoring function used here accurately models inter and intra-molecular interactions. A detailed discussion of ligand binding sites on RBD for the different types of SAs is provided in the SI, and the RBD residues involved in the binding are given in Tables S4 and S5 in the SI.

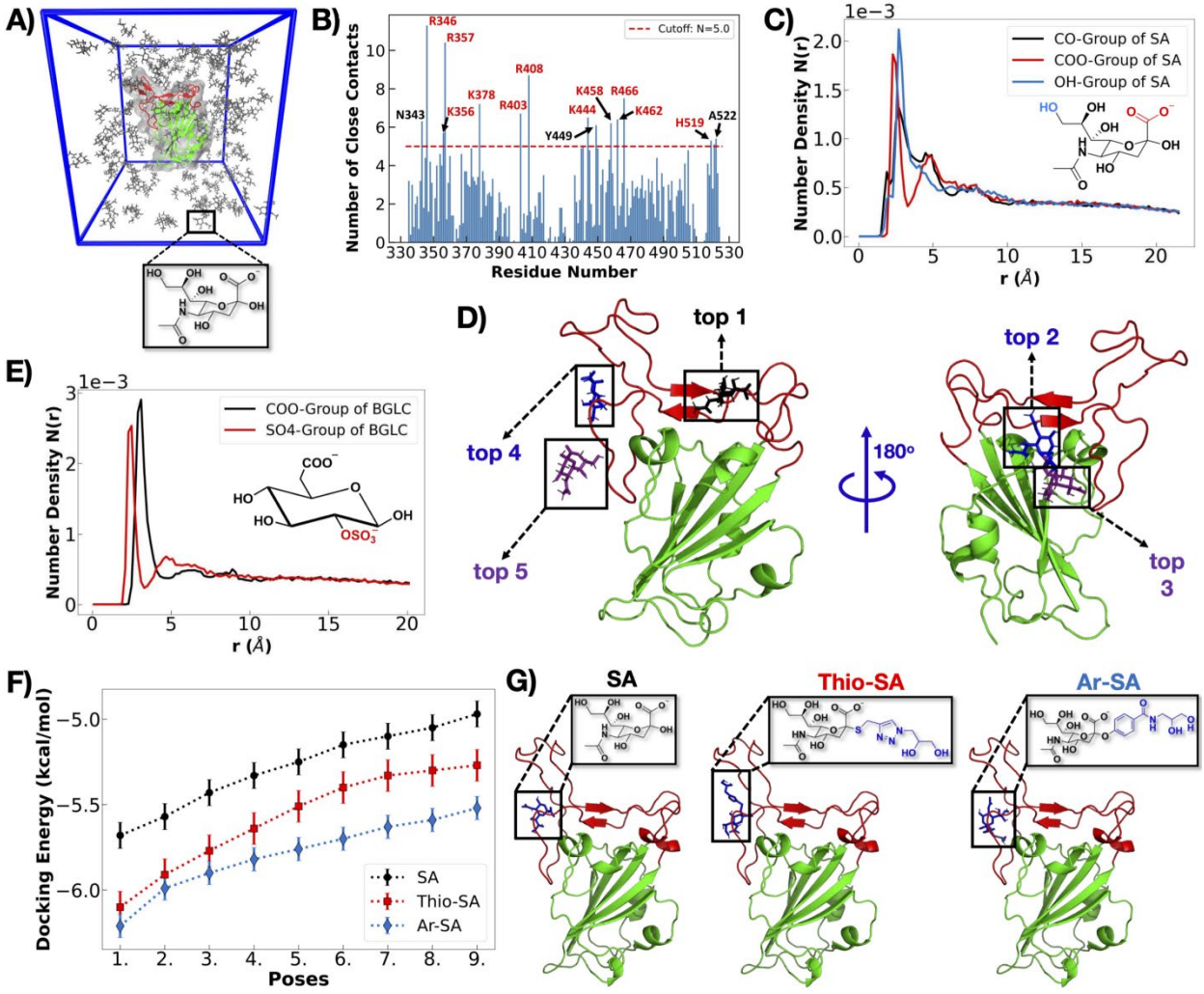

Figure 3: A) Simulation unit cell containing a single RBD (in green except the receptor binding motif, RBM, in red) and sialic acid, SA, monomers (in gray). The chemical structure of SA is shown below the simulation box. Water and ions are present in the simulation box but not shown for clarity. **B)** Number of close contacts N_c between SA ligands and different amino acid residues of RBD (averaged over simulation time of 1000 ns). Residues having $N_c > 5$ are labeled, cationic residues in red and charge neutral residues in black. **C)** Number density distribution of different functional groups (-CO, -COO^-, -OH) of SA ligands around RBD as a function of the distance *r* from the RBD surface. **D)** Snapshots of binding poses of SA obtained from the top five longest residing ligands near the RBD surface in the MD simulation (for the

details on the residue-level interactions, see Figure S19 in the SI). SA ligands shown in black, blue, or violet. RBD is shown in green except RBM (amino acid residues 438–506) in red. **E)** Number density distribution of different functional groups (-COO^-, -SO_4^-) of BGLC ligands around RBD as a function of *r*. The chemical structure of BGLC is shown in the inset. **F)** Docking interaction energies of different functionalized sialic acids (SA, Thio-SA, Ar-SA) with RBD for the top nine docking poses. Each data point and the bar represent the average value and the standard error of nine different ligand-docking studies taking different RBD conformations selected from the simulation of RBD and SA ligands. **G)** Snapshots of the best docking poses (with the RBD structure extracted from the simulation in the water-only solution after 400 ns) for the different functionalized SAs (chemical structures given on the top). RBD representation is the same as in the panel D. For the details on the residue-level interactions, see Figure S20 in the SI.

SARS-CoV-2 replication and entry inhibition in Calu-3 cells

After finding $dPG_{500}(SA)_{0.55}$ as the high affinity ligand for the SARS-Cov-2, we next tested the potential of synthesized sialylated compounds for SARS-CoV-2 B.1 (WT, D614G) infection inhibition of human lung derived Calu-3 cells.

We first investigated whether $dPG_{500}(SA)_{0.55}$ can also block entry of authentic SARS-CoV-2 virions. To determine entry efficiency, Calu-3 cells were infected with SARS-CoV-2 at 4°C to allow synchronized entry, while cells were pre- and post-treated with increasing amounts of compounds. Nucleocapsid-specific subgenomic RNA is produced during coronavirus infection early after entry in high quantities [26] and was applied to compare the entry efficiency of SARS-CoV-2 upon compound treatment. Only $dPG_{500}(SA)_{0.55}$ inhibited SARS-CoV-2 entry significantly to 18.6% at 0.5mg/ml and of 54% at 1 mg/ml, when compared to $dPG_{500}OH$ control treated Calu-3 cells (Figure 4A).

In the next step, the biological assay was set up to determine if these compounds inhibit authentic SARS-CoV-2 replication. Calu-3 cells were infected with SARS-CoV-2 isolate in presence of increasing inhibitor concentrations, which were supplied before infection and for the entire duration of the experiment. In presence of $dPG_{500}(SA)_{0.55}$ SARS-CoV-2 replication was inhibited up to 83.8% at 24 hours post-infection and to 98.9% at 48 hours post-infection at the maximum applied compound concentration of 1 mg/ml which is equivalent to 5 nM, when compared to untreated Calu-3 cells (Fig. 3 B and C). The low-density sialylated $dPG_{500}SA_{0.25}$ and aromatically modified sialylated $dPG_{500}(SAaryl)_{0.20}$ analogs showed only very weak inhibition at 24 hpi at the highest concentrations applied. A high density of SA seems to

be important for virus infection inhibition. The control compound without any SA, $dPG_{500}OH$ did not show any inhibition.

A cell viability assay was conducted to exclude the possibility that the compounds were cytotoxic. The number of viable cells remained at a constant level with increasing compound concentration at the highest dose of 1 mg/ml after 24h and 48h post treatment (Fig. S23). This confirms the specific action of the compounds.

In summary, $dPG_{500}(SA)_{0.55}$ was identified as a SARS-CoV-2 entry inhibitor in Calu-3 cells, which presumably blocks the attachment of virions to cells before specific interaction with cellular receptors occurs.

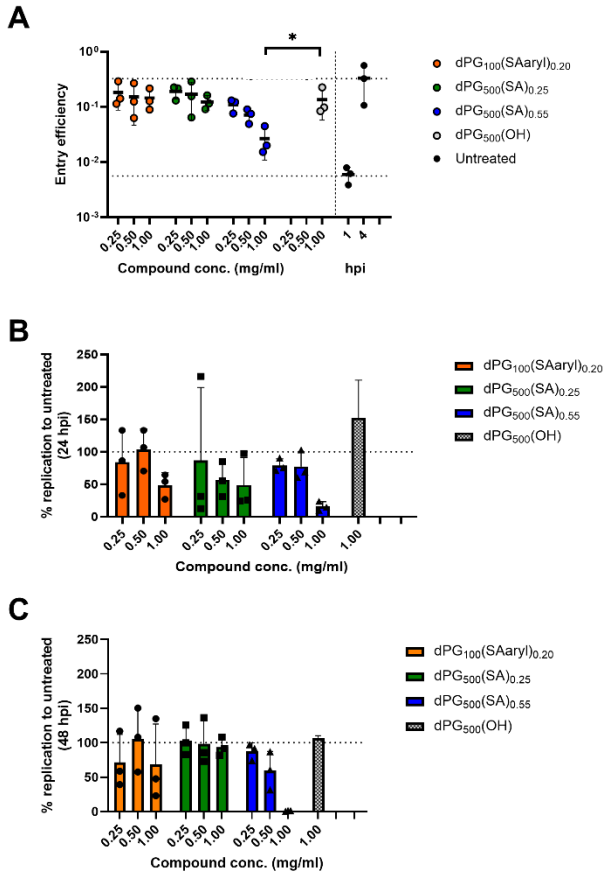

Figure 4: SARS-CoV-2 replication and entry in Calu-3 cells is inhibited by $dPG_{500}(SA)_{0.55}$. **A)** Calu-3 cells were pre- and post-treated with 0.25, 0.5, or 1 mg/ml of the indicated compounds before cells were infected with SARS-CoV-2 (MOI 2) at 4 °C to allow synchronized entry. Entry efficiency was determined from cell lysates at 4 hpi with a highly sensitive quantitative RT-PCR for nucleocapsid-specific subgenomic RNA. Entry efficiency was calculated by the delta ct method and by using the expression of cellular TATA-binding protein (TBP) as a reference. Upper dotted line represents the mean virus entry efficiency at 4 hpi and the lower dotted line represents the mean virus entry efficiency at 1 hpi. Data show means of three independently conducted experiments each performed in triplicates. **B - C)** Calu-3 cells were infected with SARS-CoV-2 (MOI 0.001) and pre- and post-treated with 0.25, 0.5 or 1 mg/ml of the indicated compounds. Virus replication was determined with an envelope-specific quantitative RT-PCR

at 24 hpi; **A)** and 48 hpi; **B)** from the supernatant of infected cells. Dotted lines represent % virus replication in untreated samples. Data shows mean values of three technical repeats together with the SD. GE: SARS-CoV-2 genome equivalents; Conc.: concentration; hpi: hours post infection; w/o: without

Cryo-TEM analysis

To visualize the binding of sialylated dPG compounds to the S-proteins of SARS-CoV-2, we cryo-prepared the ligand with the highest affinity ($dPG_{500}(SA)_{0.55}$) together with the virus particles by plunge freezing into liquid ethane to obtain a snapshot of the conditions under hydrated conditions and to analyze subsequently the viruses embedded in the amorphous ice using cryo-electron transmission microscopy (cryo-TEM). However, to ensure that the TEM projection images did not simply show overlays of virions and $dPG_{500}(SA)_{0.55}$, cryo-electron tomography (cryo-ET) combined with machine learning-based segmentation was used (Figure 5).

Fig. 5A shows the 3D reconstruction obtained from a recorded cryo tilt series. To distinguish between the S head domains (S1) of the spike proteins (the flexible and thin S2 stem is mostly not visible in the 3D reconstruction due to limited resolution) and the sialylated dPG cores, we used the machine learning algorithms of the trainable Weka (Waikato Environment for Knowledge Analysis) segmentation (more details in SI 1.13). The Segmentation was done in Fiji [25,26]. Figure 5B shows the resulting overlay of cryo-ET 3D and classified structures (green: $dPG_{500}(SA)_{0.55}$, red: spike proteins, blue: virus core).

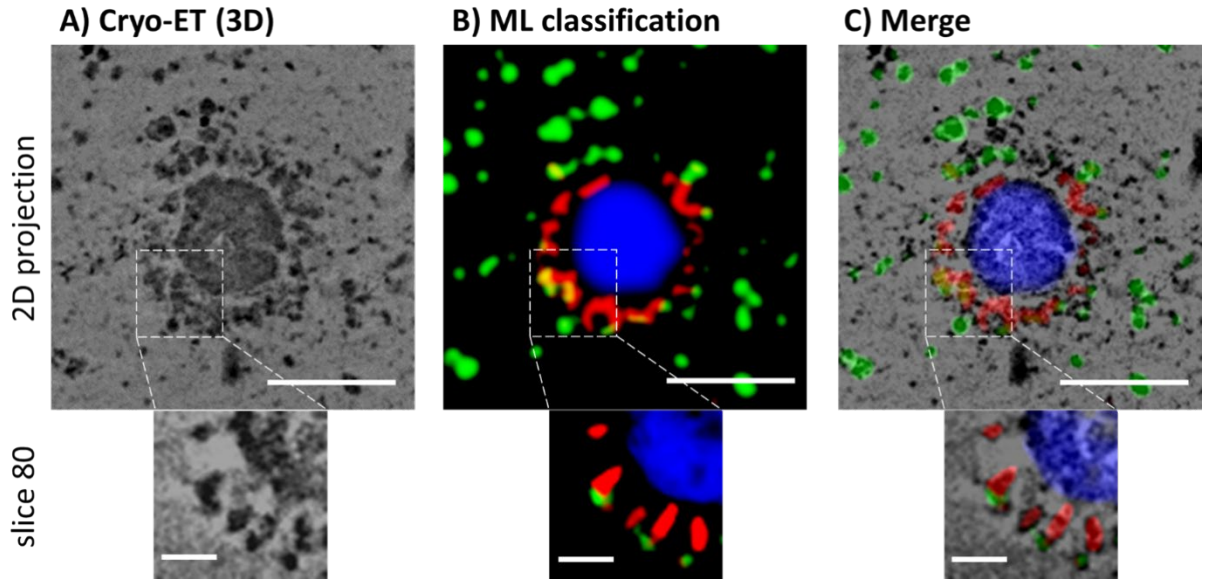

Figure 5: Cryo-ET visualization and machine learning-based segmentation of $dPG_{500}(SA)_{0.55}$ nanoparticles binding to SARS-CoV-2 spike protein RBDs. The top panels show a 2D projection of the 3D tomogram and the bottom panels show a zoom of one in-plane slice of the 3D tomogram. **A)** 3D reconstruction obtained from a recorded cryo tilt series. **B)**

Segmented 3D volume: To distinguish between the S head domains (S1) of the spike proteins (the flexible and thin S2 stem is mostly not visible in the 3D reconstruction due to limited resolution) and the sialylated dPG cores, the trainable Weka (Waikato Environment for Knowledge Analysis) segmentation classifier was applied. (dPG nanoparticles (green), spike proteins (red), and virus body (blue) highlighted). **C)** Overlay of the original image with the segmented representation. Top scale bars: 100 nm. Bottom scale bars: 25 nm.

The segmented image (panel C) reveals a clustering of nanoparticles (green) around the virus particle, particularly in areas rich with spike proteins (red). The yellow regions, indicating an overlap between red and green signals, suggest direct interaction between nanoparticles and spike proteins. This distribution pattern visualizes that the sialoside-functionalized dPG nanoparticles specifically bind to SARS-CoV-2 spike proteins.

Conclusions

This study demonstrates that a synthetic polysialoside can inhibit SARS-CoV-2 infection by direct binding with RBD on the S1 spike protein. The MD simulation, docking, and MST studies show that the direct binding of SA with RBD is not merely electrostatic but SA as a whole sugar molecule has a role in the binding interactions. The synthetic polysialoside binds at low nM concentrations (K_d = 4.78 nM) in contrast to a polysulfated analog that binds at µM concentrations (K_d = 2.46 µM). The study also outlines that high density of SA on the dendritic polymer is crucial for the SARS-CoV-2 post-infection inhibition. Infection inhibition tests performed at different time points indicate that SARS-CoV-2 infection drops dramatically by inhibiting the virus entry into Calu-3 cells in the presence of polysialoside. Overall, these findings demonstrate that high-density polysialoside represents a promising therapeutic strategy against SARS-CoV-2 infection through its nanomolar binding affinity to the RBD and effective inhibition of viral entry.

Supporting Information

Supporting Information is available free of charge. Materials and methods, detailed synthetic protocols and reaction schemes, protocols for the biological assays, MST and cryo-TEM analysis, molecular docking images, MD simulation data-analysis details, plots and tables, NMR figures, DLS plots, and cytotoxicity analysis.

Acknowledgments

We acknowledge Julian Heinz (Charité Berlin) for technical support. This work was supported by the Berlin University Alliance (BUA). SB acknowledges the funding from the Deutsche Forschungsgemeinschaft (DFG) – Project ID: 458564133, and Royal Society of Chemistry

(RSC) RG\R1\241050 and Novo Nordisk Foundation (Grant number: NNF23SA0088060). The project was realized with research infrastructure and support provided by the Research Building SupraFAB realized with funds from the Federal Government (BMBF) and the State of Berlin. SB and DL are grateful for funding from SupraFAB for the project BioSexSurf. DL is grateful for financial support from the federal ministry of education and research funded project MucPep (FKZ:13XP511). YK acknowledges the funding from the Deutsche Forschungsgemeinschaft (DFG, German Research Foundation) – Project ID 431232613 – SFB 1449/INF. We would also like to acknowledge the assistance of the Core Facility BioSupraMol. Further, we acknowledge the support provided by Deutsche Forschungsgemeinschaft Grant No. IRTG-2662 Project No. 434130070 "Charging into the future," and computing time on the HPC clusters at the Physics department, Freie Universität Berlin.

Conflict of Interest

The authors declare no conflict of interest.

References

1. WHO, COVID-19 epidemiological update – 17 September 2024. World Health Organization: **2024**; pp 1-33.
2. Liu, C.; Mendonça, L.; Yang, Y.; Gao, Y.; Shen, C.; Liu, J.; Ni, T.; Ju, B.; Liu, C.; Tang, X.; Wei, J.; Ma, X.; Zhu, Y.; Liu, W.; Xu, S.; Liu, Y.; Yuan, J.; Wu, J.; Liu, Z.; Zhang, Z.; Liu, L.; Wang, P.; Zhang, P., *Structure* **2020,** *28* (11), 1218-1224.e4. DOI 10.1016/j.str.2020.10.001.
3. Yan, R.; Zhang, Y.; Li, Y.; Xia, L.; Guo, Y.; Zhou, Q., *Science* **2020,** *367* (6485), 1444-1448. DOI 10.1126/science.abb2762.
4. Lauster, D.; Osterrieder, K.; Haag, R.; Ballauff, M.; Herrmann, A., *Frontiers in Microbiology* **2023,** *14*. DOI 10.3389/fmicb.2023.1169547.
5. Kwon, P. S.; Oh, H.; Kwon, S. J.; Jin, W.; Zhang, F.; Fraser, K.; Hong, J. J.; Linhardt, R. J.; Dordick, J. S., *Cell Discov* **2020,** *6* (1), 50. DOI 10.1038/s41421-020-00192-8.
6. Clausen, T. M.; Sandoval, D. R.; Spliid, C. B.; Pihl, J.; Perrett, H. R.; Painter, C. D.; Narayanan, A.; Majowicz, S. A.; Kwong, E. M.; McVicar, R. N.; Thacker, B. E.; Glass, C. A.; Yang, Z.; Torres, J. L.; Golden, G. J.; Bartels, P. L.; Porell, R. N.; Garretson, A. F.; Laubach, L.; Feldman, J.; Yin, X.; Pu, Y.; Hauser, B. M.; Caradonna, T. M.; Kellman, B. P.; Martino, C.; Gordts, P.; Chanda, S. K.; Schmidt, A. G.; Godula, K.; Leibel, S. L.; Jose, J.; Corbett, K. D.; Ward, A. B.; Carlin, A. F.; Esko, J. D., *Cell* **2020,** *183* (4), 1043-1057.e15. DOI 10.1016/j.cell.2020.09.033.
7. Urano, E.; Itoh, Y.; Suzuki, T.; Sasaki, T.; Kishikawa, J. I.; Akamatsu, K.; Higuchi, Y.; Sakai, Y.; Okamura, T.; Mitoma, S.; Sugihara, F.; Takada, A.; Kimura, M.; Nakao, S.; Hirose, M.; Sasaki, T.; Koketsu, R.; Tsuji, S.; Yanagida, S.; Shioda, T.; Hara, E.; Matoba, S.; Matsuura, Y.; Kanda, Y.; Arase, H.; Okada, M.; Takagi, J.; Kato, T.; Hoshino, A.; Yasutomi, Y.; Saito, A.; Okamoto, T., *Sci Transl Med* **2023,** *15* (711), eadi2623. DOI 10.1126/scitranslmed.adi2623.
8. Nie, C.; Pouyan, P.; Lauster, D.; Trimpert, J.; Kerkhoff, Y.; Szekeres, G. P.; Wallert, M.; Block, S.; Sahoo, A. K.; Dernedde, J.; Pagel, K.; Kaufer, B. B.; Netz, R. R.; Ballauff, M.; Haag, R., *Angewandte Chemie International Edition* **2021,** *60* (29), 15870-15878. DOI https://doi.org/10.1002/anie.202102717.

9. Saso, W.; Yamasaki, M.; Nakakita, S.-i.; Fukushi, S.; Tsuchimoto, K.; Watanabe, N.; Sriwilaijaroen, N.; Kanie, O.; Muramatsu, M.; Takahashi, Y.; Matano, T.; Takeda, M.; Suzuki, Y.; Watashi, K., *PLOS Pathogens* **2022,** *18* (6), e1010590. DOI 10.1371/journal.ppat.1010590.
10. Nguyen, L.; McCord, K. A.; Bui, D. T.; Bouwman, K. M.; Kitova, E. N.; Elaish, M.; Kumawat, D.; Daskhan, G. C.; Tomris, I.; Han, L.; Chopra, P.; Yang, T.-J.; Willows, S. D.; Mason, A. L.; Mahal, L. K.; Lowary, T. L.; West, L. J.; Hsu, S.-T. D.; Hobman, T.; Tompkins, S. M.; Boons, G.-J.; de Vries, R. P.; Macauley, M. S.; Klassen, J. S., *Nature Chemical Biology* **2022,** *18* (1), 81-90. DOI 10.1038/s41589-021-00924-1.
11. Baker, A. N.; Richards, S.-J.; Guy, C. S.; Congdon, T. R.; Hasan, M.; Zwetsloot, A. J.; Gallo, A.; Lewandowski, J. R.; Stansfeld, P. J.; Straube, A.; Walker, M.; Chessa, S.; Pergolizzi, G.; Dedola, S.; Field, R. A.; Gibson, M. I., *ACS Central Science* **2020,** *6* (11), 2046-2052. DOI 10.1021/acscentsci.0c00855.
12. Petitjean, S. J. L.; Chen, W.; Koehler, M.; Jimmidi, R.; Yang, J.; Mohammed, D.; Juniku, B.; Stanifer, M. L.; Boulant, S.; Vincent, S. P.; Alsteens, D., *Nature Communications* **2022,** *13* (1), 2564. DOI 10.1038/s41467-022-30313-8.
13. Bhatia, S.; Lauster, D.; Bardua, M.; Ludwig, K.; Angioletti-Uberti, S.; Popp, N.; Hoffmann, U.; Paulus, F.; Budt, M.; Stadtmüller, M.; Wolff, T.; Hamann, A.; Böttcher, C.; Herrmann, A.; Haag, R., *Biomaterials* **2017,** *138*, 22-34. DOI 10.1016/j.biomaterials.2017.05.028.
14. Mohammadifar, E.; Gasbarri, M.; Dimde, M.; Nie, C.; Wang, H.; Povolotsky, T. L.; Kerkhoff, Y.; Desmecht, D.; Prevost, S.; Zemb, T.; Ludwig, K.; Stellacci, F.; Haag, R., *Advanced Materials n/a* (n/a), 2408294. DOI https://doi.org/10.1002/adma.202408294.
15. Parshad, B.; Schlecht, M. N.; Baumgardt, M.; Ludwig, K.; Nie, C.; Rimondi, A.; Hönzke, K.; Angioletti-Uberti, S.; Khatri, V.; Schneider, P.; Herrmann, A.; Haag, R.; Hocke, A. C.; Wolff, T.; Bhatia, S., *Nano Letters* **2023,** *23* (11), 4844-4853. DOI 10.1021/acs.nanolett.3c00408.
16. Toogood, P. L.; Galliker, P. K.; Glick, G. D.; Knowles, J. R., *Journal of Medicinal Chemistry* **1991,** *34* (10), 3138-3140. DOI 10.1021/jm00114a025.
17. Bò, L.; Miotto, M.; Di Rienzo, L.; Milanetti, E.; Ruocco, G., *Front Med Technol* **2020,** *2*, 614652. DOI 10.3389/fmedt.2020.614652.
18. Lam, S. D.; Waman, V. P.; Fraternali, F.; Orengo, C.; Lees, J., *Comput Struct Biotechnol J* **2022,** *20*, 6302-6316. DOI 10.1016/j.csbj.2022.11.004.
19. Buchanan, C. J.; Gaunt, B.; Harrison, P. J.; Yang, Y.; Liu, J.; Khan, A.; Giltrap, A. M.; Le Bas, A.; Ward, P. N.; Gupta, K.; Dumoux, M.; Tan, T. K.; Schimaski, L.; Daga, S.; Picchiotti, N.; Baldassarri, M.; Benetti, E.; Fallerini, C.; Fava, F.; Giliberti, A.; Koukos, P. I.; Davy, M. J.; Lakshminarayanan, A.; Xue, X.; Papadakis, G.; Deimel, L. P.; Casablancas-Antràs, V.; Claridge, T. D. W.; Bonvin, A. M. J. J.; Sattentau, Q. J.; Furini, S.; Gori, M.; Huo, J.; Owens, R. J.; Schaffitzel, C.; Berger, I.; Renieri, A.; Study, G.-C. M.; Naismith, J. H.; Baldwin, A. J.; Davis, B. G., *Science* **2022,** *377* (6604), eabm3125. DOI doi:10.1126/science.abm3125.
20. Unione, L.; Moure, M. J.; Lenza, M. P.; Oyenarte, I.; Ereño-Orbea, J.; Ardá, A.; Jiménez-Barbero, J., *Angewandte Chemie International Edition* **2022,** *61* (18), e202201432. DOI https://doi.org/10.1002/anie.202201432.
21. Li, B.; Wang, L.; Ge, H.; Zhang, X.; Ren, P.; Guo, Y.; Chen, W.; Li, J.; Zhu, W.; Chen, W.; Zhu, L.; Bai, F., *Front Chem* **2021,** *9*, 659764. DOI 10.3389/fchem.2021.659764.
22. Banerjee, T.; Gosai, A.; Yousefi, N.; Garibay, O. O.; Seal, S.; Balasubramanian, G., *J Biomol Struct Dyn* **2024,** *42* (12), 6342-6358. DOI 10.1080/07391102.2023.2234044.
23. Monti, M.; Milanetti, E.; Frans, M. T.; Miotto, M.; Di Rienzo, L.; Baranov, M. V.; Gosti, G.; Somavarapu, A. K.; Nagaraj, M.; Golbek, T. W.; Rossing, E.; Moons, S. J.; Boltje, T. J.; van den Bogaart, G.; Weidner, T.; Otzen, D. E.; Tartaglia, G. G.; Ruocco, G.; Roeters, S. J., *The Journal of Physical Chemistry B* **2024,** *128* (2), 451-464. DOI 10.1021/acs.jpcb.3c06258.
24. Casalino, L.; Gaieb, Z.; Goldsmith, J. A.; Hjorth, C. K.; Dommer, A. C.; Harbison, A. M.; Fogarty, C. A.; Barros, E. P.; Taylor, B. C.; McLellan, J. S.; Fadda, E.; Amaro, R. E., *ACS Central Science* **2020,** *6* (10), 1722-1734. DOI 10.1021/acscentsci.0c01056.

536 25. Nie, C.; Sahoo, A. K.; Netz, R. R.; Herrmann, A.; Ballauff, M.; Haag, R., *Chembiochem* **2022,** *23*
537 (6), e202100681. DOI 10.1002/cbic.202100681.
538 26. Sawicki, S. G.; Sawicki, D. L.; Siddell, S. G., *J Virol* **2007,** *81* (1), 20-9. DOI 10.1128/JVI.01358-
539 06.

540

541

542 **TOC**

543

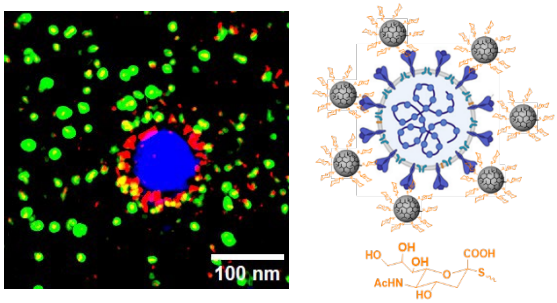

Green: dPG$_{500}$(SA)$_{0.55}$ Red: Spike proteins Blue: Virus core